Applied Catalysis A, General 673 (2024) 119589

Contents lists available at ScienceDirect

Applied Catalysis A, General

journal homepage: www.elsevier.com/locate/apcata

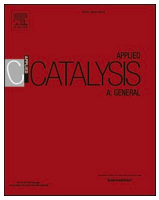

Ammonia cracking on single-atom catalysts: A mechanistic and microkinetic study

Xiuyuan Lu, Alberto Roldan *

Cardiff Catalysis Institute, School of Chemistry, Cardiff University, Main Building, Park Place, Cardiff CF10 3AT, UK

ARTICLE INFO

Keywords:
Single-atom catalysts (SACs)
Hydrogen
Ammonia
Computational catalysis
Microkinetics

ABSTRACT

Ammonia cracking has been identified as a crucial step to unlocking a sustainable economy. Using the density functional theory, we modeled transition metal single-atom catalysts (SACs) supported on graphene and nitrogen-modified graphene to investigate the catalytic NH_3 cracking process. The results showed that (i) N-modified graphene secures the transition metal atoms (M) stronger than C-matrixes, and (ii) structures with three anchoring nitrogens (MN_3) are more reactive than MN_4 ones. On IrN_3 and RuN_3 SAC models, the N_2 evolution determines the total rate, while, on RhN_3-SAC, it is the NH_3 dehydrogenation. Temperature-programmed desorption simulations on SACs showed variations compared to extended metal surfaces. Batch reactor simulations were employed to balance the sequence of elementary steps as a function of the temperature, revealing the overall NH_3 cracking activity. Results suggested IrN_3 and RhN_3 are strong candidates for NH_3 cracking at temperatures as low as 230 °C.

1. Introduction

Hydrogen (H_2) is a viable and sustainable long-term energy vector that can address increasing global energy demands, and its utilization is compatible across vehicles, industries, and heating and cooling applications [1,2]. However, H_2 is highly volatile and flammable, and its distribution using pipes presents challenges due to leakage [3]. Instead, ammonia (NH_3) is a potential hydrogen vector with high hydrogen density (17.6 wt%), carbon-free, and suitable for storage at low pressure (~7.5 atm at 300 K) [4,5].

The endothermic NH_3 cracking process could provide a steady H_2 supply for clean energy technologies such as fuel cells [6]. However, the cost and low energy efficiency of current NH_3 cracking catalysts hinder their implementation on a large scale [5,7,8]. The literature on NH_3 cracking using heterogeneous catalysts is extensive; recent reviews can be found elsewhere [9–15]. These traditional catalysts are commonly based on costly late transition metals. The initial capital of these catalysts can be significantly reduced using single-atom catalysts (SACs) [16]. SACs present the highest level of atom efficiency as each atom participates in independent catalytic reactions.

SACs have recently attracted attention in the nitrogen reduction reaction (NRR), i.e., the reverse process of ammonia cracking [17–21]. Wang and co-workers found that Au SACs supported in g-C_3N_4 have higher NRR electrocatalytic activity and selectivity than Au(211) surfaces [22]. The Au/g-C_3N_4 faradaic efficiency (FE) is 11.1 %, lower than for Ru SACs on N-doped carbon (FE = 29.6 %), which also benefits from reducing the hydrogen poisoning and the H_2 evolution reaction compared with Ru nanoparticles [23]. A density functional theory (DFT) investigation found that the Ru atom in SAC structures is firmly anchored to the carbon matrix and presents a similar NRR limiting potential independently of the carbon-based materials, e.g., C_2N, T-C_3N_4, and γ-graphene [24]. Based on the fact that Fe is the industrial catalyst for the Haber-Bosch process and is present in the nitrogenase enzymes, [25]. Li et al. modeled the highly spin-polarised FeN_3 center and found it to adsorb and activate N_2 [26]. Lü et al. also reported a FeN_4 structure to be NRR active [27]. Alternative transition metal atoms such as Sc, V, Mn, Co, Y, and Mo were embedded in graphene and tested as NRR catalysts, [26,28,29] the latest suggesting a Mars–van Krevelen reaction mechanism [29].

We considered the previous NRR observations and catalytic results on supported metal particles [7,8,10,13] to investigate the NH_3 cracking reaction on transition metal SACs supported in carbon and nitrogen-doped carbon structures using systematic DFT calculations. We went beyond the information in mechanistic energy profiles and implemented the derived information in microkinetic batch reactor models and temperature-programmed desorption (TPD) simulations,

* Corresponding author.
E-mail address: roldanmartineza@cardiff.ac.uk (A. Roldan).

https://doi.org/10.1016/j.apcata.2024.119589
Received 16 November 2023; Received in revised form 15 January 2024; Accepted 29 January 2024
Available online 1 February 2024

providing a multiscale approach to the computational results.

2. Computational details

We employed the Vienna Ab-initio Simulation Package (VASP) to model the NH_3 cracking mechanisms on transition metals single-atom catalysts (Fe, Co, Ni, Zn, Ru, Rh, and Ir) anchored on defective and pyridinic nitrogen-doped graphene layers [30,31]. The spin-polarised revised Perdew-Burke-Ernzerhof (RPBE) method of the generalized gradient approximation (GGA) was adopted to describe the exchange and correlation energies with a plane-wave kinetic cutoff of 500 eV [32]. Spin alignments were fully relaxed to the lowest energy configuration, avoiding any constraint to the system [33]. Non-spherical contributions to atomic cores from the electron density gradient were represented by the projector augmented wave (PAW) [34]. The zero-damping DFT-D3 method was used to describe long-range interactions [35]. The optimized convergence thresholds of internal forces and electronic relaxation were set to 0.02 eV/Å and 10^{-5} eV, respectively. A $3 \times 3 \times 1$ k-spacing Monkhorst-Pack grid sampled the Brillouin zone with a smearing broadening of 0.2 eV for bulk metals, 0.1 eV for SACs, and 0.02 eV for isolated molecules [36]. Bader charges were calculated to assign partial charges to specific atoms [37]. A negative value of the charge indicates the accumulation of electron density.

SACs' surfaces were represented by a graphite *p(6 × 6)* supercell slab model with a single atomic layer thickness. We added 15 Å of vacuum perpendicular to the slab to avoid spurious interaction with periodic images. Dipole correction perpendicular to the surface was applied upon the adsorption of any species. The strength of binding (E_b) a single metal atom on a defective carbon or nitrogen-doped carbon matrix was evaluated using Eq. (1).

$$E_b = E_{SAC} - E_g - E_m \tag{1}$$

Where E_{SAC}, E_g, and E_m represent the energies of the supported SAC, the graphitic support (with or without N-doping), and the metal atom within the metal bulk in its most stable crystal structure. The last two energies define the binding reference energy. Table S1 of the Supplementary Information shows the optimized metal bulk lattice parameters. The molecular adsorption energies (E_{ads}) were defined by Eq. (2), and the relative energies (ΔE) along the energy profiles were calculated by Eq. (3).

$$E_{ads} = E_{system} - E_{SAC} - E_{molecule} \tag{2}$$

$$\Delta E = E_{system} + \frac{n}{2} * E_{H_2} - E_{SAC} - E_{NH_3} \tag{3}$$

Where E_{system} is the total energy of the adsorbed structure, E_{SAC} and $E_{molecule}$ denote the energy of the clean SAC and isolated molecular adsorbate, respectively. E_{NH_3} and E_{H_2} are the energies of isolated ammonia and hydrogen molecules. The last three terms are the reference energy maintained along all the reaction profiles. The half energy of a hydrogen molecule refers to the energy of one H atom, and n is the number of H dissociated from NH_3. The reaction energy (E_r) of each step was given by the energy difference between the final state (FS) and the initial state (IS) (Eq. (4)). An exothermic reaction step is associated with a negative E_r. The transition states (TS) were determined using the climb-image nudged elastic band (ci-NEB) combined with the improved dimer method (IDM), ensuring a unique imaginary frequency along the reaction coordinate [38–40]. Vibrational frequency calculations were carried out by constructing and diagonalizing the Hessian matrix, built from finite displacements of atomic positions of 0.05 Å in length. Only displacements of the adsorbates were regarded, i.e. the adsorbate vibrations were treated decoupled from the TM-SACs surface, since test calculations considering them yielded negligible changes in the gained vibrational frequencies at an exceedingly high computational cost. We defined the forward and reverse activation barriers (E_a) as the energy difference between TS and IS and between TS and FS, respectively (Eq. (5) and Eq. (6)).

$$E_r = E^{FS} - E^{IS} \tag{4}$$

$$E_a^{forward} = E^{TS} - E^{IS} \tag{5}$$

$$E_a^{reverse} = E^{TS} - E^{FS} \tag{6}$$

3. Results and discussion

3.1. Transition metal anchoring sites

We modeled single- and double-carbon vacancies in graphene and nitrogen-modified graphene (g-N_3 and g-N_4) supports [41]. The vacant carbon and nitrogen sites are known to coordinate with metal atoms to saturate their dangling bonds [42–44]. Fig. 1 represents the different structures according to the metal anchoring site. The significant surface properties of the SACs with the modeled transition metals are summarised in Table 1.

The binding energy of a transition metal atom within the nitrogen-modified graphene is stronger than in the non-doped defective carbon matrix, which explains the SACs' synthetic protocols [43,45]. The binding energies in Table 1 show the SAC's formation of 4-coordinated structures (MX_4) to be thermodynamically more favourable than 3-coordinated ones (MX_3). Generally, the metal on MN_3 protrudes from the support plane driven by the N lone pair electrons (Fig. 1), affecting the M-N bonds and angles compared to the M-C bond. The resulting geometries in MN_4 and MC_4 are similar. Fe, Co, and Ni metal atoms have a stronger affinity with nitrogen than noble metals such as Ru, Rh, and Ir, meaning the former SACs are more stable than noble metal ones. A positive E_b value indicates a thermodynamic driving force for the atoms to merge into a metallic bulk; our results on less durable SACs align with previous observations [42,44,46].

3.2. Ammonia cracking

3.2.1. Surface species

Based on the thermodynamically favourable metal interaction with

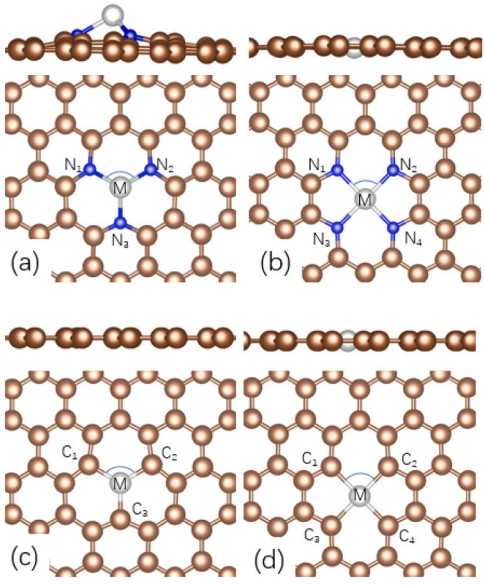

Fig. 1. Top and side schematic representations of SACs' anchoring sites: (a) MN_3, (b) MN_4, (c) metal on graphene single-vacancy (MC_3), and (d) metal on graphene double-vacancy (MC_4). Khaki, blue, and silver spheres represent carbon, nitrogen, and transition metal atoms.

Table 1
Geometric details and binding energies of modelled SACs. Label d(MX) (X = N, C) is the bond length between metal (M) and nitrogen (N) or carbon (C) atoms, $\angle X_1MX_2$ indicates the angle between the MX bonds, and E_b designates the binding energy.

	Item	Fe	Co	Ni	Zn	Ru	Rh	Ir
MN_3	d(MN)(Å)	1.891	1.857	1.874	2.028	1.931	2.055	2.054
	$\angle N_1MN_2(^\circ)$	94.8	96.8	95.1	83.9	90.9	81.4	82.0
	E_b(eV)	0.51	-0.17	0.27	-0.14	2.22	2.06	3.3
MC_3	d(MC)(Å)	1.675	1.667	1.693	1.775	1.754	1.751	1.769
	$\angle C_1MC_2(^\circ)$	120.0	120.0	118.1	115.4	120.0	119.9	120.0
	E_b(eV)	0.90	0.77	1.20	2.97	3.38	2.49	3.08
MN_4	d(MN)(Å)	1.898	1.88	1.885	1.967	1.954	1.946	1.957
	$\angle N_1MN_2(^\circ)$	88.6	88.2	88.3	88.2	89.0	89.3	89.9
	E_b(eV)	-2.47	-2.6	-3.14	-2.26	0.07	-1.25	-0.65
MC_4	d(MC)(Å)	1.917	1.894	1.874	1.939	1.858	1.865	1.887
	$\angle N_1MN_2(^\circ)$	87.4	88.0	87.9	87.6	81.9	82.1	83.0
	E_b(eV)	-0.48	-0.30	-0.94	-0.78	1.05	0.34	0.59

the N-doped graphene, we investigated several non-equivalent NH_x(x = 0–3) and H adsorption conformations on MN_3 and MN_4 SACs, and N and C sites neighbouring the M centres (M= Fe, Co, Ni, Zn, Ru, Rh, and Ir). A detailed description of adsorptions far from the metal centre can be found in Ref. [41]. The most likely adsorption mode is on top of the transition metal atoms. The adsorption preference is explained by the partial occupation of hybridized *sd* metal orbitals interacting with the NH_3 lone pair electrons, supporting the electron back donation and activation of the N–H bond; see the MN_x (x = 3 and 4) electronic details in Table 2 and density of states in Figs. S1-S7 [47].

A favourable NH_3 adsorption is essential to initiate catalytic molecular cracking. Table 3 summarises the adsorption energies of the adsorbents, i.e., NH_3, N_2, and H_2. The NH_3 adsorption is generally more advantageous on MN_3 than on MN_4. Another thermodynamic drive for ammonia cracking is the desorption of N_2 and H_2, which should be more likely than their atoms remaining on the SAC. In this case, MN_4 structures predominate. The interaction strength and distance between the adsorbate and the adsorption site are commonly correlated on heterogeneous catalysts [48]. Table S2 shows this is not the case with these SACs, as their interaction is confined to a single atom.

Another factor to consider in promising catalysts is a smooth energy profile along the reaction mechanism, i.e., intermediate species interacting neither too weak nor too strong [49]. The focus on the first dehydrogenation is crucial as it has been identified previously as a rate-limiting step. Fig. 2 illustrates the relative reaction energies (ΔE) starting from the clean SAC and isolated NH_3 molecule; adsorbed structures are schematically represented in Figs. S8-S21. The thermodynamic profiles show that only ZnN_3, RuN_3, RhN_3, IrN_3 and ZnN_4 present favourable NH_3 adsorption and dehydrogenation. Most MN_3 SACs fail on the last dehydrogenation step, leading to adsorbed N. It differs from the MN_4 SACs, which, except ZnN_4, are not able to stabilize NH_2, meaning that the first NH_3 dehydrogenation thermodynamically hinders the reaction progress. The presence of NH_2 on a SAC is only likely on ZnN_3, although these energies are close on NiN_3, IrN_3, RuN_3, and RhN_3 cases. The NH_2 and NH dehydrogenations on FeN_3, CoN_3, and NiN_3 are thermodynamically impeded, explained by the small size of these atoms and the highly localized electrons at the Fermi energy Fig. S3.

Considering the kinetic aspects is also crucial to identifying efficient catalysts; a generalized representation of the mechanism is shown in Fig. 3. From the shortlisted SACs, the activation energies on ZnN_3 are 2.13, 3.46, and 2.71 eV for the first, second, and third dehydrogenation, implying a kinetically hindered process. Overall, only three transition metal SAC candidates are not frustrated by NH_3 dehydrogenation, IrN_3, RuN_3, and RhN_3, of which reaction energy profiles are shown in Fig. 4.

The energy profiles (Fig. 4) include NH_3 adsorption, dehydrogenations, and nitrogen recombination and evolution, all linked through the transition state determining the kinetic feasibility of the overall endothermic NH_3 cracking; note that ΔE is not at standard conditions and includes the internal molecular energies leading to ΔE > ΔH of NH_3 formation ($\Delta H_f^o = -46.1 kJ{\cdot}mol^{-1}$). IrN_3 and RuN_3 profiles clearly display the highly endothermic nitrogen recombination, which is easier to achieve on RhN_3. Another significant feature is the high activation energies for NH dehydrogenation on RuN_3 and RhN_3.

3.2.2. Reaction Thermochemistry

The differences in Gibbs free energy (ΔG_r) and activation energy (ΔG_a) of each elementary surface reaction were determined to consider temperature effects on the NH_3 cracking process [48]. We investigated the possibility of N_2 recombination through a Mars-van Krevelen mechanism but found energy barriers (>3 eV). Therefore, the surface NH_3 decomposition on 3 N-coordinated noble metals sites follows a Langmuir–Hinshelwood stepwise dehydrogenation (R1: $NH_3^* + * \longrightarrow NH_2^* + H^*$; R3: $NH_2^* + * \longrightarrow NH^* + H^*$; R5: $NH^* + * \longrightarrow N^* + H^*$) and N_2 and H_2 formations (R7: $2N^* \longrightarrow N_2^* + *$; R9: $2H^* \longrightarrow H_2^* + *$), which ΔG_r and ΔG_a are represented as a function of the temperature in Fig. 5; for completeness, ΔG_r and ΔG_a of the other SACs are represented in Fig. S22. The dehydrogenation transition states (TS1-TS5) are shown in the schematic diagrams of Fig. S8-**21**.

On IrN_3, the energy barriers for the stepwise dehydrogenation reactions are ~1 eV, more likely than on RuN_3 (ΔG_a~ 1.5 eV). Despite this, the endothermic N recombination reaction (R7) is the rate-determining step with a barrier energy of ~2 eV (~1.5 eV for RuN_3), hindering the continuous generation of N_2. Contrarily, on RhN_3, the NH dehydrogenation (R5) controls the overall reaction rate with a ΔG_a~ 1.5 eV, although it is practically isoenergetic. The N_2 recombination (R7) on RhN_3 is just ΔG_a~ 0.6 eV.

Based on the reaction and activation free energies, we derived the rate law's pre-exponential factors (ν) and reaction constants (k), see Table S3. Fully aligned with the discussion above, the reaction constant for N_2 formation (R7) on IrN_3 and RuN_3 are very small (k(300 K)~ 10^{-20} and 10^{-16} s^{-1}), whereas, on RhN_3, it is the NH dehydrogenation (R5; k (300 K)~10^{-14} s^{-1}). Comparing the dehydrogenation constants (R1, R3, R5) against these in opposite directions, i.e., hydrogenation (R2, R4, R6), shows that the equilibrium is shifted towards the dehydrogenation of NH_x (x = 1–3), highlighting these three SACs catalytic potential for NH_3 cracking.

Table 2
Electronic details of modelled MN_3 and MN_4 SACs, including the metal Bader charge (q) and spin density (s), and the total surface magnetic moment (M_s).

	Item	Fe	Co	Ni	Zn	Ru	Rh	Ir
MN_3	q(e^-)	-1.06	-0.93	-0.97	-0.79	-1.12	-0.72	-0.75
	s(μ_B)	3.28	2.17	1.31	0.64	0.00	1.21	1.08
	$M_s(\mu_B)$	3.35	2.34	1.50	0.69	0.00	1.75	2.23
MN_4	q(e^-)	-1.20	-1.07	-1.05	-1.28	-1.36	-0.95	-1.15
	s(μ_B)	2.01	0.87	0.00	0.00	1.67	0.05	0.42
	$M_s(\mu_B)$	1.60	0.94	0.00	0.00	0.00	0.40	1.00

Table 3
ZPE corrected adsorption energies (E_{ads}) of molecular species on MN_3 and MN_4 SACs (M = Fe, Co, Ni, Zn, Ru, Rh, and Ir).

	Adsorbate	Fe	Co	Ni	Zn	Ru	Rh	Ir
MN_3	NH_3	-1.02	-0.44	-0.84	-0.17	-1.19	-1.11	-1.28
	N_2	-0.75	-0.13	-0.79	-0.14	-1.28	-1.18	-0.46
	H_2	-0.46	-0.35	-0.41	-0.09	-0.78	-0.71	0.09
MN_4	NH_3	0.61	-0.57	0.05	-1.07	-0.20	-0.13	-0.74
	N_2	-0.14	-0.11	-0.10	-0.18	-0.12	-0.13	-0.12
	H_2	-0.11	0.00	-0.03	-1.18	-0.09	-0.10	-0.11

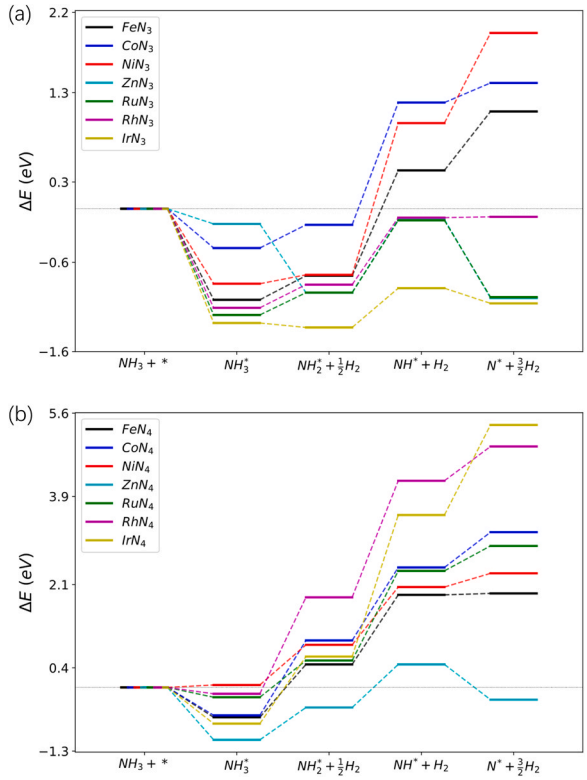

Fig. 2. Thermodynamic profile for the adsorption and dehydrogenation of NH_3 on (a) MN_3 and (b) MN_4.

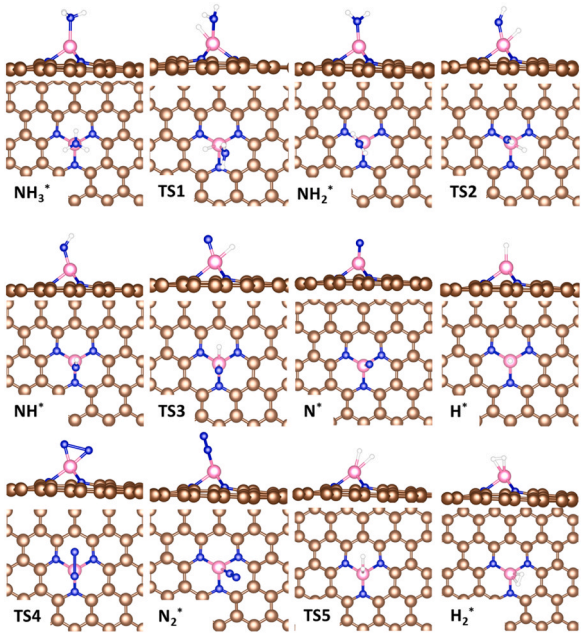

Fig. 3. Top and side schematic representations of the NH_3 cracking reaction surface intermediates (denoted with *) on SACs, including transition states (TS). Khaki, blue, white, and silver spheres represent carbon, nitrogen, hydrogen, and transition metal atoms.

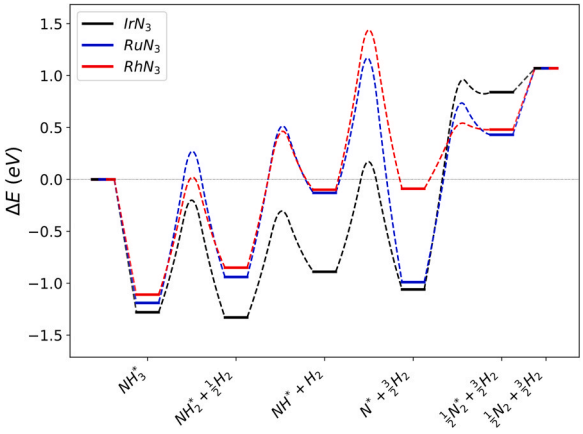

Fig. 4. Energy profiles for the ammonia cracking reaction on IrN_3, RuN_3, and RhN_3 single-atom catalysts.

3.3. Microkinetics

We calculated the partition functions of each gaseous and surface species involved in the process to derive their thermodynamic properties as functions of the temperature [50]. For instance, the entropic terms include, for molecules, the electronic, translational, and rotational contributions besides the 3 N-6 vibrations in the vibrational partition function; for surface species, entropy includes frustrated translational and rotational contributions within the 3 N vibrations in the partition function. We implemented the temperature-dependent energies in the Eyring, Evans, and Polanyi approximation to compute the reaction constants of all elementary surface reactions [51–53]. These constants were used to construct a kinetic model of the reversible NH_3 cracking reaction based on a microcanonical ensemble within the transition state theory framework, the details of which can be found elsewhere [48,54]. The solutions for the system of ordinary differential equations, i.e. the variation of each species with time, were derived by propagating it to equilibrium (Fig. S23).

3.3.1. Temperature-programmed desorption (TPD)

The molecular desorptions from catalysts are crucial to ensure the availability of the active site and turnover; thus, we simulated the temperature-programmed desorption to identify trends and temperatures in which desorption occurs. We found significant differences between the N_2 and H_2 TPD on IrN_3, RuN_3, and RhN_3 SACs compared with their extended metals (Fig. 6). The H_2 desorption occurs on metallic Ir(111) at ~300 K, [34] whereas, on IrN_3-SAC, it desorbs at a temperature below 200 K. Nevertheless, both catalysts present similar N_2 desorption curves expanding from 550–750 K. The N_2 and H_2 TPD curves on RuN_3-SAC shifted to the lower temperature by ~150 K and

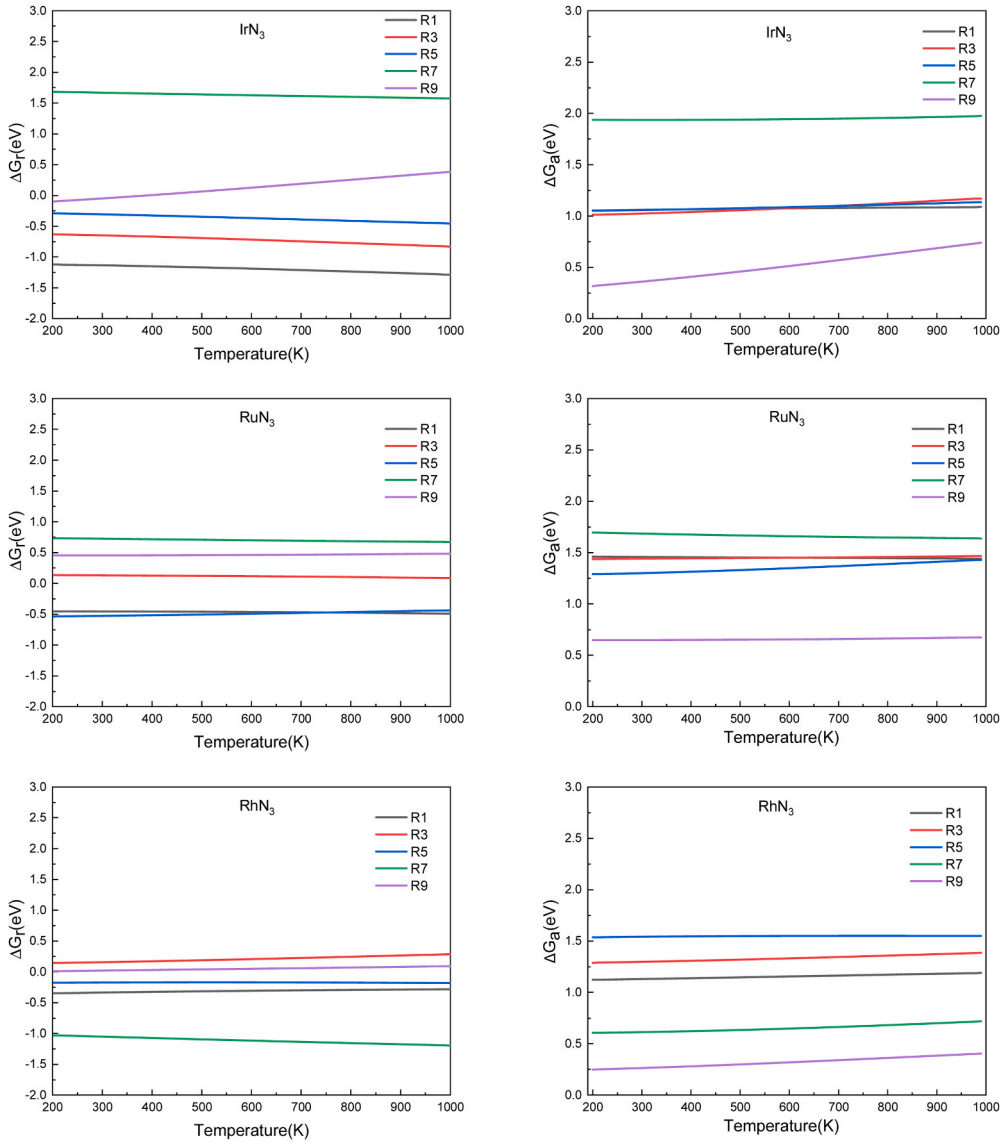

Fig. 5. Reaction (ΔG_r) and activation (ΔG_a) free energies of each elementary step in ammonia dehydrogenation (R1, R3, R5) and N_2 and H_2 formations (R7 and R9) on IrN_3, RuN_3, and RhN_3 as a function of the temperature.

~25 K with respect to the ones reported on the hcp-Ru(0001) surface. [34] These results prove the effective desorption of SACs compared to traditional metal catalysts as they minimize the lateral interaction with co-adsorbed species. The low desorption temperatures of H_2 (~300 K) and N_2 (~400 K) on the RhN_3 SAC suggest a significant NH_3 cracking conversion at mild temperatures upon NH dehydrogenation.

3.3.2. *Batch reactor simulations*

We have simulated the ratio between molecular species and active sites on IrN_3, RuN_3, and RhN_3 SACs as a function of the temperature and the reaction time. The equilibrium between SAC-adsorbed and gas NH_3 is established at low temperatures until the dehydrogenation and molecular recombination energy barriers are surmounted upon increasing temperatures. The steady-state ratio (χ) of NH_3, N_2, and H_2 as functions of temperature after 600 s of reaction is shown in Fig. 7. Note that 600 s is enough to reach equilibrium.

The H_2 evolution occurs between 425 and 550 K, resulting from an initial NH_3 decomposition. On IrN_3, the content of H_2 in the gas phase rises at a low temperature (~425 K) and quickly reaches a plateau at around 500 K, indicating the saturation of active sites by NH_x ($x < 3$) species. On RuN_3, the H_2 does not reach an apparent plateau within the temperature range. It is related to the competing H_2 adsorption and the slight increase in the probability of desorbing with the increasing temperature. RhN_3 behaves similarly to IrN_3, although the $\chi(H_2)$ is ~1.5 lower due to the difficulty of overtaking the endothermic NH_2 dehydrogenation. Despite this, RhN_3 has an earlier (T~ 700 K) but slower H_2 desorption than IrN_3 (T~ 750 K). The main H_2 desorption is followed by N_2 evolution at T~ 725 K (~800 K on IrN_3), which competes with molecular adsorptions. N_2 desorption does not arise from RuN_3, confirming the inability of this SAC to regenerate the catalytic site. Our results predict the NH_3 regeneration at ~500 K, which is in agreement with the NH_3 synthesis experiment on the Ru SACs [42].

The predominant species on the surfaces after 600 s of reaction within a temperature range of 200–1000 K are plotted in Fig. 8. At low temperatures (< 400 K), the adsorbed NH_3 molecule accommodates on the three catalysts. At 500 K, NH_2 becomes the dominant species on the IrN_3 surface, but it is quickly replaced by N as the temperature rises, displaying the slight endothermic path between dehydrogenation steps, see Fig. 4. The strong adsorption of N on IrN_3 hinders the reactivity of the site until the temperature reaches ~800 K, promoting the N_2 evolution. The dominant species on RuN_3 during the reaction are NH_2 and N at 460–520 K and > 520 K, respectively. The N ad-atoms remain on the

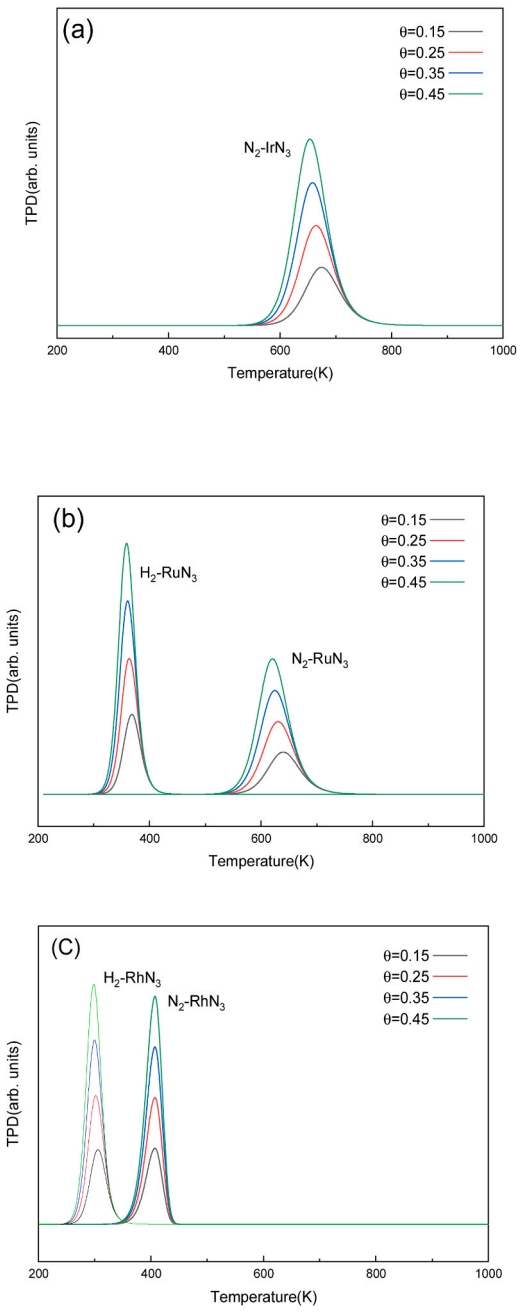

Fig. 6. Simulated N_2 and H_2 TPD on (a) IrN_3, (b) RuN_3, and (c) RhN_3 at different initial atomic coverages (θ in ML) with the heating rate of 1 K/min.

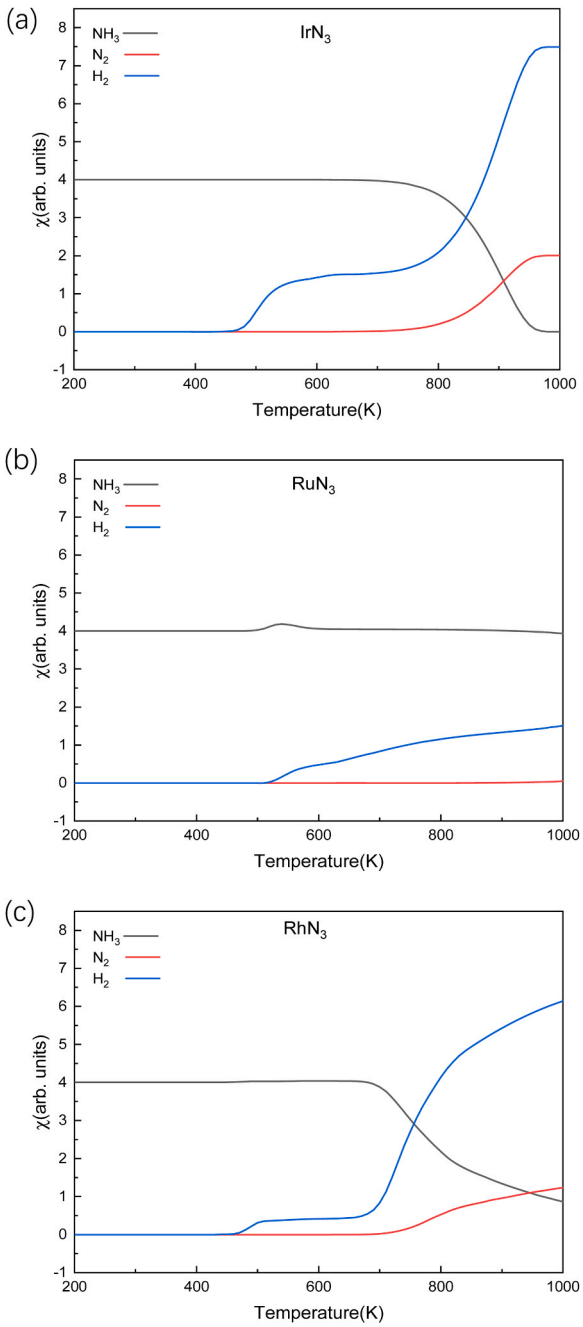

Fig. 7. The steady-state ratio (χ) of molecular NH_3, N_2, and H_2 as functions of temperature upon NH_3 cracking catalyzed by (a) IrN_3, (b) RuN_3, and (c) RhN_3 on batch reactor simulations. The initial simulated conditions are an NH_3 ratio of 5:1 with the surface and a reaction time of 600 s.

metal site due to the high energy barrier for their recombination (R7). NH_2 is the predominant species on the RhN_3-SAC at the temperature range of 500–720 K with a maximum coverage of 0.9 ML at 680 K, related to the endothermic R3 step (~0.75 eV). Once overtaken at ~700 K, molecular N_2 takes most of the metal centres due to its favourable re-adsorption on RhN_3. It is worth mentioning that although R5 on RhN_3 has the highest activation energy of the energy profile, it is an apparent rate-limiting because NH does not accumulate on the surface at the temperature at which R3 is surmounted.

4. Conclusion

Single transition metal atoms supported on clean and nitrogen-modified graphene were simulated as MC_3, MC_4, MN_3, and MN_4 (M= Fe, Co, Ni, Ir, Ru, Rh, and Zn). The results show that nitrogen-modified graphene has a more robust interaction with metal atoms than vacancy graphene, providing high resistance to metal sintering and leaching. We investigated the NH_3 cracking reaction mechanism on these SACs supported on N-modified graphene and found that the most likely adsorption site is directly on top of the metal atom. The relative energies suggested that MN_3 structures are more active than MN_4 as the former enhances the electron back-donation, activating the N–H bond. The results confirmed that, on SACs, the first NH_3 dehydrogenation and the N_2 evolution are the rate-determining steps for ammonia cracking. The most promising candidates were those formed by Ir, Ru, and Rh metals. The free energies of molecular and adsorbed species were calculated between 200 and 1000 K for a thermochemical analysis, revealing slight variations of reaction and activation free energies with the temperature.

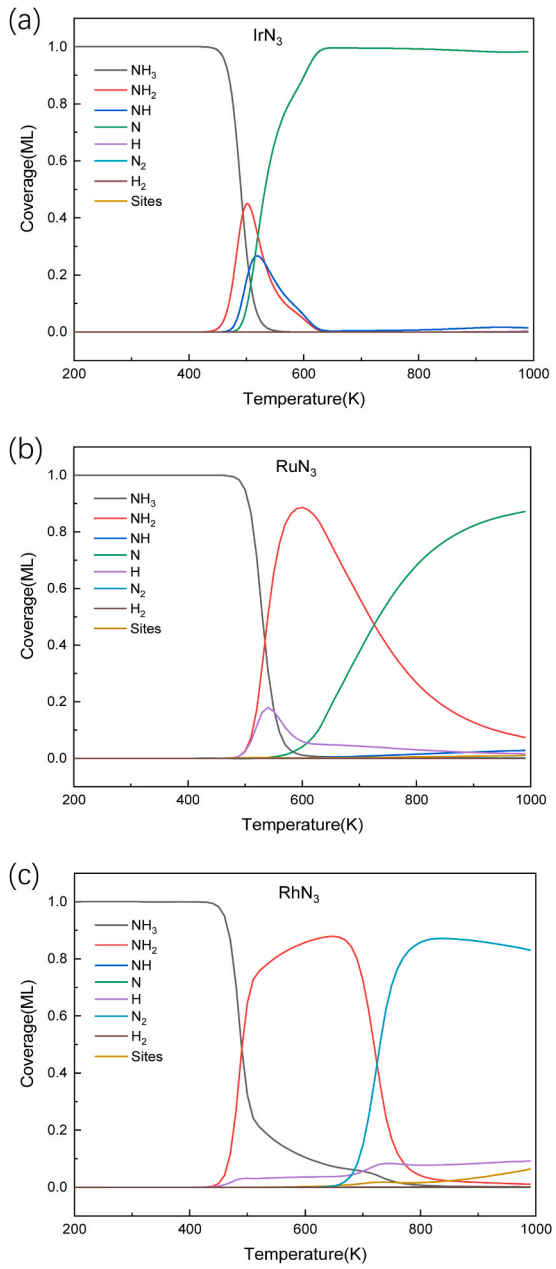

Fig. 8. Surface species distribution upon NH_3 cracking on (a) IrN_3, (b) RuN_3, and (c) RhN_3 surface at the 200–1000 K temperature range and 600 s of reaction.

We implemented the free energies in temperature-programmed desorption simulations, finding that desorption temperatures from SACs are smaller than those on extended surfaces. Batch reaction simulations probed IrN_3 and RhN_3 SACs as promising catalysts for NH_3 cracking, being the latest active at lower temperatures than the former.

CRediT authorship contribution statement

Xiuyuan Lu: Formal analysis, Investigation, Visualization, Writing – original draft. **Alberto Roldan:** Conceptualization, Data curation, Formal analysis, Project administration, Resources, Supervision, Validation, Writing – review & editing.

Declaration of Competing Interest

The authors declare the following financial interests/personal relationships which may be considered as potential competing interests: Alberto Roldan reports financial support was provided by Engineering and Physical Sciences Research Council. Xiuyuan Lu reports financial support was provided by China Scholarship Council.

Data availability

I have shared the link to my data in the Acknowledgements section.

Acknowledgements

X. Lu acknowledges the China Scholarship Council and Cardiff University for the overseas student scholarship (CSC No. 201806370221). We are grateful for funding from the Engineering and Physical Sciences Research Council (EP/P005845/1). Via our membership of the UK's HEC Materials Chemistry Consortium, funded by EPSRC (EP/R029431), this work used the UK Materials and Molecular Modelling Hub for computational resources, MMM Hub, which is partially funded by EPSRC (EP/T022213). We also acknowledge the Isambard 2 UK National Tier-2 HPC Service (http://gw4.ac.uk/isambard/) operated by GW4 and the UK Met Office, funded by EPSRC (EP/T022078/1), and supercomputing Wales for access to the Hawk HPC facility, part-funded by the European Regional Development Fund via the Welsh Government. All data created during this research are available from the University of Cardiff Research Portal orca websites http://doi.org/10.17035/d.2023.0263893141.

Appendix A. Supporting information

Supplementary data associated with this article can be found in the online version at doi:10.1016/j.apcata.2024.119589.

References

[1] A. Pareek, R. Dom, J. Gupta, J. Chandran, V. Adepu, P.H. Borse, Insights into renewable hydrogen energy: Recent advances and prospects, Mater. Sci. Energy Technol. 3 (2020) 319–327.
[2] H.A. Lara-García, J.A. Mendoza-Nieto, H. Pfeiffer, L. Torrente-Murciano, COx-free hydrogen production from ammonia on novel cobalt catalysts supported on 1D titanate nanotubes, Int. J. Hydrogen Energy 44 (2019) 30062–30074.
[3] IEA, The Future of Hydrogen: Seizing today's opportunities, Propos. Doc. Jpn. Pres. G20 (2019) 203.
[4] G. Wang, A. Mitsos, W. Marquardt, Conceptual design of ammonia-based energy storage system: System design and time-invariant performance, AIChE J. 63 (2017) 1620–1637.
[5] A. Valera-Medina, R. Banares-Alcantara. Techno-Economic Challenges of Green Ammonia as an Energy Vector, 1st ed., Elsevier, 2021.
[6] S. Chiuta, R.C. Everson, H.W.J.P. Neomagus, P. Van Der Gryp, D.G. Bessarabov, Reactor technology options for distributed hydrogen generation via ammonia decomposition: a review, Int. J. Hydrogen Energy 38 (2013) 14968–14991.
[7] K. Fothergill, S. Greenwood, J. Makepeace, I. Wilkinson, C. Jackson, T. Davenne, C. Makhloufi, I. Wilkinson, K. Fothergill, S. Greenwood, N. Kezibri, Ammonia to green hydrogen project, Feasibility Study 33 (2020) 1–70.
[8] O. Grasham, V. Dupont, T. Cockerill, M.A. Camargo-Valero, M.V. Twigg, Hydrogen: via reforming aqueous ammonia and biomethane co-products of wastewater treatment: environmental and economic sustainability, Sustain. Energy Fuels 4 (2020) 5835–5850.
[9] I. Lucentini, X. Garcia, X. Vendrell, J. Llorca, Review of the decomposition of ammonia to generate hydrogen, Ind. Eng. Chem. Res. 60 (2021) 18560–18611.
[10] S.F. Yin, B.Q. Xu, X.P. Zhou, C.T. Au, A mini-review on ammonia decomposition catalysts for on-site generation of hydrogen for fuel cell applications, Appl. Catal. A Gen. 277 (2004) 1–9.
[11] M. Aziz, A. TriWijayanta, A.B.D. Nandiyanto, Ammonia as effective hydrogen storage: a review on production, storage and utilization, Energies 13 (2020) 3062.
[12] A. Afif, N. Radenahmad, Q. Cheok, S. Shams, J.H. Kim, A.K. Azad, Ammonia-fed fuel cells: a comprehensive review, Renew. Sustain. Energy Rev. 60 (2016) 822–835.
[13] T.E. Bell, L. Torrente-Murciano, H2 production via ammonia decomposition using non-noble metal catalysts: a review, Top. Catal. 59 (2016) 1438–1457.
[14] T. Zhang, H. Miyaoka, H. Miyaoka, T. Ichikawa, Y. Kojima, Review on ammonia absorption materials: metal hydrides, halides, and borohydrides, ACS Appl. Energy Mater. 1 (2018) 232–242.
[15] K. Ogasawara, T. Nakao, K. Kishida, T.N. Ye, Y. Lu, H. Abe, Y. Niwa, M. Sasase, M. Kitano, H. Hosono, Ammonia decomposition over CaNH-supported Ni catalysts via an NH2–vacancy-mediated mars-van krevelen mechanism, ACS Catal. 11 (2021) 11005–11015.

[16] Y. Qiu, X. Peng, F. Lü, Y. Mi, L. Zhuo, J. Ren, X. Liu, J. Luo, Single-atom catalysts for the electrocatalytic reduction of nitrogen to ammonia under ambient conditions, Chem. - Asian J. 14 (2019) 2770–2779.
[17] L. Han, X. Liu, J. Chen, R. Lin, H. Liu, L.U. Fang, S. Bak, Z. Liang, S. Zhao, E. Stavitski, J. Luo, R.R. Adzic, H.L. Xin, Atomically dispersed molybdenum catalysts for efficient ambient nitrogen fixation, Angew. Chem. - Int. Ed. 58 (2019) 2321–2325.
[18] G. Kyriakou, M.B. Boucher, A.D. Jewell, E.A. Lewis, T.J. Lawton, A.E. Baber, H. L. Tierney, M. Flytzani-Stephanopoulos, E.C.H. Sykes, Isolated metal atom geometries as a strategy for selective heterogeneous hydrogenations, Science 335 (*80-*.) (2012) 1209–1212.
[19] Y. Yao, S. Zhu, H. Wang, H. Li, M. Shao, A spectroscopic study on the nitrogen electrochemical reduction reaction on gold and platinum surfaces, J. Am. Chem. Soc. 140 (2018) 1496–1501.
[20] Z. Geng, Y. Liu, X. Kong, P. Li, K. Li, Z. Liu, J. Du, M. Shu, R. Si, J. Zeng, Achieving a record-high yield rate of 120.9 μgNH3mgcat.−1h−1 for N2 electrochemical reduction over Ru single-atom catalysts, Adv. Mater. 30 (2018) 1803498.
[21] Q. Qin, T. Heil, M. Antonietti, M. Oschatz, Single-site gold catalysts on hierarchical N-doped porous noble carbon for enhanced electrochemical reduction of nitrogen, Small Methods 2 (2018) 1800202.
[22] X. Wang, W. Wang, M. Qiao, G. Wu, W. Chen, T. Yuan, Q. Xu, M. Chen, Y. Zhang, X. Wang, J. Wang, J. Ge, X. Hong, Y. Li, Y. Wu, Y. Li, Atomically dispersed Au1 catalyst towards efficient electrochemical synthesis of ammonia, Sci. Bull. 63 (2018) 1246–1253.
[23] H. Tao, C. Choi, L.X. Ding, Z. Jiang, Z. Han, M. Jia, Q. Fan, Y. Gao, H. Wang, A. W. Robertson, S. Hong, Y. Jung, S. Liu, Z. Sun, Nitrogen fixation by Ru single-atom electrocatalytic reduction, Chem 5 (2019) 204–214.
[24] Y. Cao, Y. Gao, H. Zhou, X. Chen, H. Hu, S. Deng, X. Zhong, G. Zhuang, J. Wang, Highly efficient ammonia synthesis electrocatalyst: single Ru atom on naturally nanoporous carbon materials, Adv. Theory Simul. 1 (2018) 1800018.
[25] S.L. Foster, S.I.P. Bakovic, R.D. Duda, S. Maheshwari, R.D. Milton, S.D. Minteer, M. J. Janik, J.N. Renner, L.F. Greenlee, Catalysts for nitrogen reduction to ammonia, Nat. Catal. 1 (2018) 490–500.
[26] X.F. Li, Q.K. Li, J. Cheng, L. Liu, Q. Yan, Y. Wu, X.H. Zhang, Z.Y. Wang, Q. Qiu, Y. Luo, Conversion of dinitrogen to ammonia by FeN3-embedded graphene, J. Am. Chem. Soc. 138 (2016) 8706–8709.
[27] F. Lü, S. Zhao, R. Guo, J. He, X. Peng, H. Bao, J. Fu, L. Han, G. Qi, J. Luo, X. Tang, X. Liu, Nitrogen-coordinated single Fe sites for efficient electrocatalytic N2 fixation in neutral media, Nano Energy 61 (2019) 420–427.
[28] J. Liu, X. Kong, L. Zheng, X. Guo, X. Liu, J. Shui, Rare earth single-atom catalysts for nitrogen and carbon dioxide reduction, ACS Nano 14 (2020) 1093–1101.
[29] N. Saeidi, M.D. Esrafili, J.J. Sardroodi, Electrochemical reduction of N2 to NH3 using a Co-atom stabilised on defective N-doped graphene: a computational study, ChemistrySelect 4 (2019) 12216–12226.
[30] G. Kresse, J. Furthmüller, Efficiency of ab-initio total energy calculations for metals and semiconductors using a plane-wave basis set, Comput. Mater. Sci. 6 (1996) 15–50.
[31] T. Bucko, J. Hafner, S. Lebegue, J.G. Angyan, Improved description of the structure of molecular and layered crystals: ab initio DFT calculations with van der waals corrections, J. Phys. Chem. A 114 (2010) 11814–11824.
[32] B. Hammer, L.B. Hansen, J.K. Nørskov, Improved adsorption energetics within density-functional theory using revised Perdew-Burke-Ernzerhof functionals, Phys. Rev. B 59 (1999) 7413–7421.
[33] Q. Dang, S. Tang, T. Liu, X. Li, X. Wang, W. Zhong, Y. Luo, J. Jiang, Regulating electronic spin moments of single-atom catalyst sites via single-atom promoter tuning on S-vacancy MoS 2 for efficient nitrogen fixation, J. Phys. Chem. Lett. 12 (2021) 8355–8362.
[34] G. Kresse, D. Joubert, From ultrasoft pseudopotentials to the projector augmented-wave method, Phys. Rev. B 59 (1999) 1758.
[35] S. Grimme, S. Ehrlich, L. Goerigk, Effect of the damping function in dispersion corrected density functional theory, J. Comput. Chem. 32 (2011) 1456–1465.
[36] H.J. Monkhorst, J.D. Pack, Special points for Brillouin-zone integrations, Phys. Rev. B 13 (1976) 5188–5192.
[37] R.F.W. Bader, Atoms in molecules, Acc. Chem. Res. 18 (1985) 9–15.
[38] G. Henkelman, B.P. Uberuaga, H. Jonsson, H. Jónsson, A climbing image nudged elastic band method for finding saddle points and minimum energy paths, J. Chem. Phys. 113 (2000) 9901–9904.
[39] G. Henkelman, H. Jónsson, A dimer method for finding saddle points on high dimensional potential surfaces using only first derivatives, J. Chem. Phys. 111 (1999) 7010–7022.
[40] G. Henkelman, H. Jonsson, H. Jónsson, Improved tangent estimate in the nudged elastic band method for finding minimum energy paths and saddle points, J. Chem. Phys. 113 (2000) 9978–9985.
[41] X. Lu, A. Roldan, Are carbon-based materials good supports for the catalytic reforming of ammonia? J. Phys. Chem. C 125 (2021) 15950–15958.
[42] Y. Peng, B. Lu, S. Chen, Carbon-supported single atom catalysts for electrochemical energy conversion and storage, Adv. Mater. 30 (2018) 1801995.
[43] H. Fei, J. Dong, Y. Feng, C.S. Allen, C. Wan, B. Volosskiy, M. Li, Z. Zhao, Y. Wang, H. Sun, P. An, W. Chen, Z. Guo, C. Lee, D. Chen, I. Shakir, M. Liu, T. Hu, Y. Li, A. I. Kirkland, X. Duan, Y. Huang, General synthesis and definitive structural identification of MN4C4 single-atom catalysts with tunable electrocatalytic activities, Nat. Catal. 1 (2018) 63–72.
[44] M.B. Gawande, P. Fornasiero, R. Zbořil, Carbon-based single-atom catalysts for advanced applications, ACS Catal. 10 (2020) 2231–2259.
[45] A. Zitolo, N. Ranjbar-Sahraie, T. Mineva, J. Li, Q. Jia, S. Stamatin, G.F. Harrington, S.M. Lyth, P. Krtil, S. Mukerjee, E. Fonda, F. Jaouen, Identification of catalytic sites in cobalt-nitrogen-carbon materials for the oxygen reduction reaction, Nat. Commun. 8 (1) (2017) 11.
[46] C. Rivera-Cárcamo, P. Serp, Single atom catalysts on carbon-based materials, ChemCatChem 10 (2018) 5058–5091.
[47] J. Long, X. Fu, J. Xiao, The rational design of single-atom catalysts for electrochemical ammonia synthesis: Via a descriptor-based approach, J. Mater. Chem. A 8 (2020) 17078–17088.
[48] X. Lu, J. Zhang, W.K. Chen, A. Roldan, Kinetic and mechanistic analysis of NH3decomposition on Ru(0001), Ru(111) and Ir(111) surfaces, Nanoscale Adv. 3 (2021) 1624–1632.
[49] P. Sabatier, Hydrogénations et déshydrogénations par catalyse, Ber. der Dtsch. Chem. Ges. 44 (1911) 1984–2001.
[50] I. Chorkendorff, J.W. Niemantsverdriet, Concepts of Modern Catalysis and Kinetics, Wiley, Weinheim, FRG, 2003.
[51] M.G. Evans, M. Polanyi, Some applications of the transition state method to the calculation of reaction velocities, especially in solution, Trans. Faraday Soc. 31 (1935) 875–893.
[52] H. Eyring, The activated complex in chemical reactions, J. Chem. Phys. 3 (1935) 107–115.
[53] H. Eyeing, The activated complex and the absolute rate of chemical reactions, Chem. Rev. 17 (1935) 65–77.
[54] A.H. Motagamwala, J.A. Dumesic, Microkinetic modeling: a tool for rational catalyst design, Chem. Rev. 121 (2021) 1049–1076.